JOURNAL OF MATERIALS SCIENCE **36** (2001) 1149–1160

Non-stoichiometry, grain boundary transport and chemical stability of proton conducting perovskites

S. M. HAILE, G. STANEFF, K. H. RYU
Materials Science, California Institute of Technology, Pasadena, CA 91125, USA
E-mail: smhaile@caltech.edu

The interrelationship between defect chemistry, non-stoichiometry, grain boundary transport and chemical stability of proton conducting perovskites (doped alkaline earth cerates and zirconates) has been investigated. Non-stoichiometry, defined as the deviation of the A : M molar ratio in AMO_3 from 1 : 1, dramatically impacts conductivity, sinterability and chemical stability with respect to reaction with CO_2. In particular, alkaline earth deficiency encourages dopant incorporation onto the A-atom site, rather than the intended M-atom site, reducing the concentration of oxygen vacancies. Transport along grain boundaries is, in general, less favorable than transport through the bulk, and thus only in fine-grained materials does microstructure impact the overall electrical properties. The chemical stability of high conductivity cerates is enhanced by the introduction of Zr. The conductivity of $BaCe_{0.9-x}Zr_xM_{0.1}O_3$ perovskites monotonically decreases with increasing x (increasing Zr content), with the impact of Zr substitution increasing in the order M = Yb → Gd → Nd. Furthermore, the magnitude of the conductivity follows the same sequence for a given zirconium content. This result is interpreted in terms of dopant ion incorporation onto the divalent ion site.

1. Introduction

Doped perovskite oxides, such as $BaCeO_3$, $BaZrO_3$, and $SrCeO_3$, have been widely studied in recent years as potential proton conducting electrolytes for a variety of electrochemical devices, including fuel cells, electrolysis cells, and hydrogen pumps [1]. The introduction of a trivalent dopant such as Gd into $BaCeO_3$ is normally assumed to occur as per Equation 1 (written in Kroeger-Vink notation).

$$2Ce_{Ce}^{x} + O_O^x + Gd_2O_3 \Rightarrow 2Gd_{Ce}' + V_O^{\bullet\bullet} + 2CeO_2. \quad (1)$$

The dopant dissolution mechanism leads to the creation of oxygen vacancies. Subsequent exposure to humid atmospheres is presumed to lead to the incorporation of protons as per Equation 2.

$$H_2O(gas) + V_O^{\bullet\bullet} + O_O \Rightarrow 2OH_O^{\bullet}. \quad (2)$$

The protons introduced by this manner are generally not bound to any particular oxygen ion, but are instead free to migrate from one ion to the next. This easy migration results in the high proton conductivity (as high as $10^{-2}\ \Omega^{-1}cm^{-1}$ at 500 °C) observed in these oxides [2]. Furthermore, proton transport dominates the overall electrical transport to temperatures of approximately 600 °C; the proton transport number of $BaCe_{0.95}Sm_{0.05}O_3$, for example, is ∼0.85 at this temperature [3]. At higher temperatures, both oxide ion transport and electron transport become significant.

Despite the flurry of attention directed towards these materials, proton conducting perovskite oxides present both outstanding scientific and technological challenges. In the present paper we highlight, in particular, issues of (1) defect chemistry and non-stoichiometry (2) grain boundary transport, and (3) chemical stability.

2. Non-stoichiometry

The influence of non-stoichiometry in AMO_3 perovskites, where non-stoichiometry is defined as the deviation of the molar ratio of A to M from 1 : 1, on proton transport was first recognized by Kreuer *et al.* [4]. Experimentally, these authors observed that doped barium cerate compositions with a slight barium deficiency exhibited significantly lower conductivities than stoichiometric compositions, whereas barium excess led to high conductivity. In these experiments it was further noted that barium deficiency could be achieved either from an adjustment of the initial composition, or by exposing the material to an elevated temperature for prolonged periods of time and inducing BaO vaporization. It was concluded from these observations that dopants such as Gd^{3+} substitute not only for Ce^{4+} as given in Equation 1, but also for Ba^{2+} as per Equation 3

$$2Ba_{Ba} + Gd_2O_3 \Rightarrow 2Gd_{Ba}^{\bullet} + O_i'' + 2BaO_{excess} \quad (3a)$$

or

$$2Ba_{Ba} + V_O^{\bullet\bullet} + Gd_2O_3 \Rightarrow 2Gd_{Ba}^{\bullet} + O_O^x + 2BaO_{excess} \quad (3b)$$

and thereby lead to the presence of excess barium oxide. In this manner, the similar effect of doping with a trivalent ion and introducing excess Ba could be rationalized. It was further proposed that excess BaO exists at the grain boundaries of dense polycrystalline barium cerate and is responsible for proton transport, particularly at low water adsorption levels. It is noteworthy that dopant ion incorporation by Equation 3 also results in a concentration of oxygen vacancies that is lower than if Gd incorporation took place only on the intended Ce site.

Since this first important work by Kreuer *et al.* [4] the present authors and others have systematically examined the role of non-stoichiometry on the properties of barium cerate and to some extent strontium cerate and strontium zirconate [5–8]. In addition, theoretical studies have been carried out on the zirconates to establish the energies of various defect incorporation or formation reactions [9]. The results of these studies can shed light on the defect chemistry of the cerates. While there is some discrepancy between the experimental results of various groups, there appears to be consensus in selected arenas, as described below.

2.1. BaO excess

In materials containing an excess of Ba, the overall stoichiometry may be maintained via a BaO rich grain boundary phase, as originally proposed by Kreuer, or by the direct incorporation of excess BaO into the bulk crystal structure. Three possible defect reactions can be considered to describe direct incorporation;

$$\mathrm{BaO} \rightarrow \mathrm{Ba}_\mathrm{i}^{\bullet\bullet} + \mathrm{O}_\mathrm{i}'' \tag{4}$$

$$\mathrm{BaO} \rightarrow \mathrm{Ba}_\mathrm{Ba} + \mathrm{O}_\mathrm{O} + \mathrm{V}_\mathrm{Ce}'''' + 2\mathrm{V}_\mathrm{O}^{\bullet\bullet} \tag{5}$$

and

$$2\mathrm{BaO} \rightarrow \mathrm{Ba}_\mathrm{Ba} + \mathrm{Ba}_\mathrm{Ce}'' + 2\mathrm{O}_\mathrm{O} + \mathrm{V}_\mathrm{O}^{\bullet\bullet}. \tag{6}$$

Examination of barium-rich cerates (both doped and undoped) by X-ray diffraction has not revealed the presence of any secondary crystalline phases. Compositions examined to date include $1.1\mathrm{BaO}\bullet\mathrm{CeO_2}$ [4]; $1\text{-}1.04\ \mathrm{BaO}\bullet0.85\mathrm{CeO_2}\bullet0.075\mathrm{Gd_2O_3}$,$1\text{-}1.04\mathrm{BaO}\bullet\mathrm{CeO_2}$ [5]; $1\text{-}1.2\mathrm{BaO}\bullet0.9\mathrm{CeO_2}\bullet0.05\mathrm{Y_2O_3}$ [7], $1\text{-}1.1\mathrm{BaO}\bullet\mathrm{CeO_2}$ [8], $\mathrm{BaO}\bullet0.9\mathrm{CeO_2}\bullet0.025\mathrm{Y_2O_3}$, $\mathrm{BaO}\bullet0.85\mathrm{CeO_2}\bullet 0.05\mathrm{Y_2O_3}$, $\mathrm{SrO}\bullet0.9\mathrm{CeO_2}\bullet0.025\mathrm{Y_2O_3}$, $\mathrm{SrO}\bullet0.85\mathrm{Ce O_2}\bullet0.025\mathrm{Y_2O_3}$, $1.05\mathrm{SrO}\bullet\mathrm{CeO_2}$ [6], $1\text{-}1.04\mathrm{BaO}\bullet\mathrm{ZrO_2}$ and $1\text{-}1.04\mathrm{BaO}\bullet0.85\mathrm{ZrO_2}\bullet0.075\mathrm{Y_2O_3}$ [present work]. The absence of diffraction peaks associated with a barium rich compound does not preclude the presence of such a phase in the intergranular regions of barium cerate as a material such as BaO or $\mathrm{Ba(OH)_2}$ would be expected to be amorphous. Unfortunately, attempts to directly examine intergranular regions, by electron microscopy for example, have yielded inconclusive results. In some instances an amorphous phase and/or enhanced barium content is observed (even in stoichiometric compositions), whereas in others, the grain boundaries are free of secondary phases, Table I. It appears, therefore, that the state of the grain boundaries in proton conducting perovskites is highly dependent on the precise nature of the dopant, the dopant concentration, and perhaps the processing route. Nevertheless, it is clear that an intergranular phase is not a prerequisite for either high proton conductivity or excess BaO accommodation, and we now turn our attention to the bulk incorporation reactions given in Equations 4–6.

TABLE I Results of transmission electron microscopy investigations of the grain boundary regions of proton conductivity perovskites

Host material	Dopant	Concentration	Intergranular phase?	Source
$BaCeO_3$	Nd	5%	no	Nowick & Du [10]
	Nd	10%	no	Nowick & Du [10]
	Nd	12%	yes[a]	Nowick & Du [10]
	Gd	10%	no	Nowick & Du [10]
	Gd	10%	no	Haile *et al.* [11]
	Gd	15%	no	Haile *et al.* [11]
$SrCeO_3$	Yb	5%	no	Krug *et al.* [12]
	Yb	5%	yes[b]	Lutyen *et al.* [13]

Barium excess has a number of consequences in addition to inducing high conductivity in undoped barium cerate: (1) the bulk lattice constant increases in both doped and undoped compositions [5, 7, 8], (2) the water uptake increases [5], (3) the sinterability generally increases [5, 6], and (4) the material stability decreases [5, 6]. An increase in sinterability may result from an increase in diffusion coefficients due to higher defect concentrations as implied by reactions (4)–(6). Alternatively, the presence of an intergranular liquid phase at high temperatures may be responsible for enhanced densification. The first two consequences (lattice constant and water content variations), in contrast, are, without question, due to changes to the bulk crystalline structure of barium cerate (the total water content is too great to be accounted for by H_2O dissolution at grain boundaries). An increase in water uptake is consistent with both reactions (5) and (6), and of these two, reaction (6) is more likely to induce increases in cell volumes. An examination of the defect energetics established for $CaZrO_3$ and $SrZrO_3$ [9] further indicates that the creation of A-O interstitial pairs, reaction (4), is unlikely. In calcium zirconate the energy per defect is ∼5.6 eV, whereas in $SrZrO_3$ it is ∼8 eV. In contrast, the energies associated with reaction (5) for calcium and strontium zirconate are ∼1 and ∼0.7 eV/defect, respectively. Details of the calculations that yield these values are provided in an appendix. Point defects analogous to those relevant in reaction (6), in which the divalent ion occupies the tetravalent ion site, have not been analyzed. However, one might expect the energies to be comparable to that of reaction (5) given the ionic radii of Ba^{2+} and Ce^{4+}, 1.36 Å, and 0.80 Å, respectively (values for 6-fold coordination) [14].

Incorporation of excess barium oxide via either reaction (5) or (6) would suggest that barium rich compositions should, in all cases, exhibit higher conductivities than stoichiometric compositions. While an increase in conductivity is indeed observed for Ba-rich *undoped* compositions, it is not uniformly observed for those containing a dopant. For example, Shima and Haile

observed a monotonic decrease in conductivity in Gd-doped barium cerate with increasing barium content at low temperatures and under H_2O saturated atmospheres [5]. At high temperatures, however, the trend was reversed. In Y-doped barium cerate, Guan *et al.* noted that barium excess increased the conductivity at low dopant concentrations (5%) but lowered it at higher dopant concentrations (10%) [6]. A similar reduction in conductivity upon increasing Ba content was observed by Ma *et al.* for 10% Y doped barium cerate under a wide variety of atmospheres [7]. It is certainly evident that further studies are necessary to clarify the impact of alkaline earth metal excess on ion transport in doped perovskite oxides.

2.2. BaO deficiency

The first studies of barium-deficient, undoped barium cerate demonstrated that the perovskite structure does not tolerate significant barium deficiencies [5]. That is, compositions rich in cerium showed the presence of cerium oxide as measured by X-ray powder diffraction. Subsequent investigations by Ma *et al.* suggest that a single phase perovskite can be obtained from compositions deficient in barium by as much as 5% [8]. While this latter observation is supported, to some extent, by the relatively low defect energies associated with Ca-O and Sr-O Schottky-type defect pairs in alkaline earth zirconates [9], single-phase barium cerate of composition $Ba_{0.95}CeO_3$ is, in the present authors' opinion, rather optimistic. Recent studies of Ba deficient barium zirconate are in agreement with the earlier results for barium cerate. Samples of nominal compositions $0.96–1.01BaO{\bullet}ZrO_2$ were prepared by solid state reaction (milled $BaCO_3$ and ZrO_2 calcined at 1400 °C for 30 hours) and examined by X-ray powder diffraction. The measured diffraction patterns are shown in Fig. 1a. It is evident that even the nominally stoichiometric composition contains an impurity phase. Its presence is likely a result of BaO loss during calcination, and demonstrates

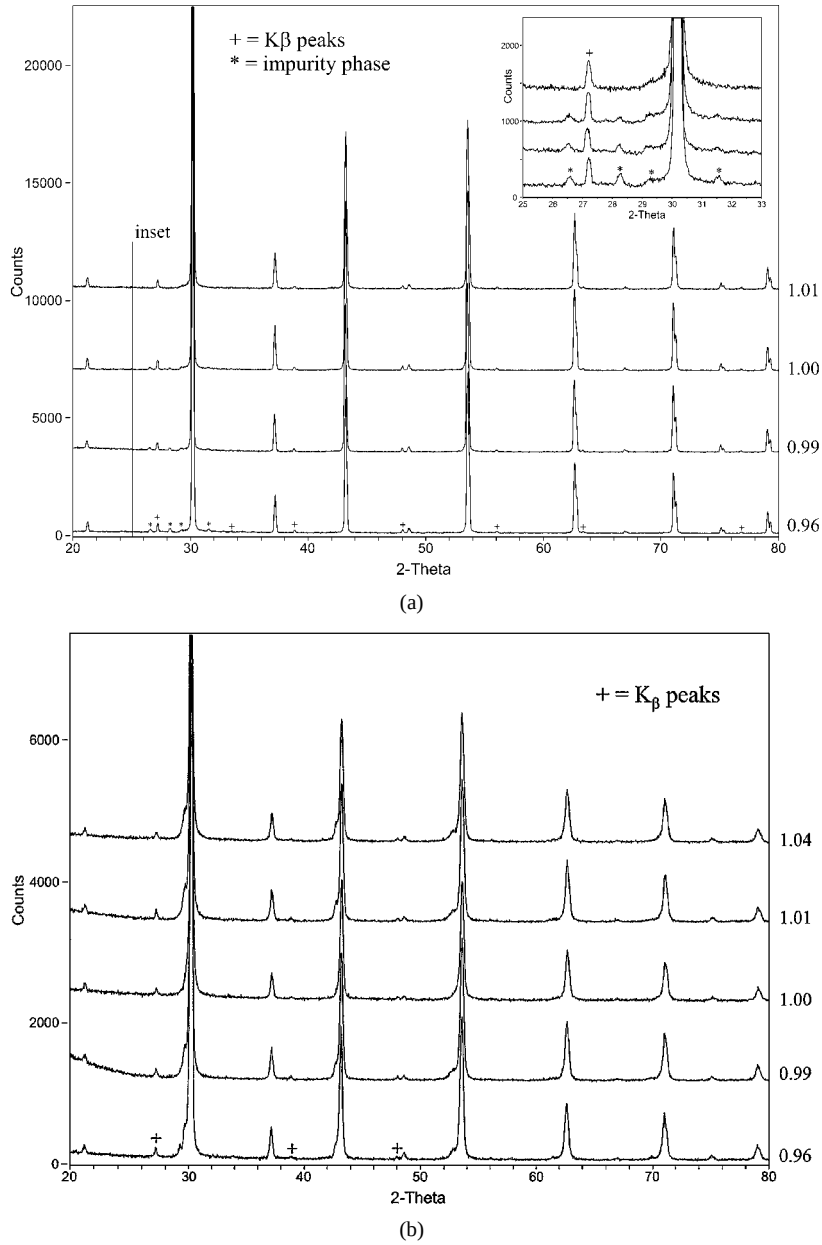

Figure 1 X-ray powder diffraction patterns of non-stoichiometric perovskites: (a) $xBaO{\bullet}ZrO_2$; (b) $xBaO{\bullet}0.85ZrO_2{\bullet}0.075Y_2O_3$.

that the perovskite phase will not withstand significant A-site deficiencies.

Whereas undoped perovskites will not accommodate alkaline earth deficiencies, doped compositions remain single phase even under highly non-stoichiometric conditions (4–10 mole% Ba/Sr deficient, depending on the dopant ion). As an example, the diffraction patterns of $0.96–1.04BaO•0.85ZrO_2•0.075Y_2O_3$ (prepared from solid state reaction as described above for undoped compositions) are shown in Fig. 1b. The difference in behavior between doped and undoped compositions implies that the mechanism by which non-stoichiometry is accommodated involves the defect chemistry of the dopant ion. Specifically, we proposed previously [5] that some portion of the dopant ions may reside on the Ba rather than Ce site, in accordance with reaction (7):

$$2Ba_{Ba} + 2O_O + Gd'_{Ce} + V_O^{\bullet\bullet} \rightarrow Gd^{\bullet}_{Ba} + 2BaO \uparrow \quad (7a)$$

$$2CeO_2 + Gd'_{Ce} + V_O^{\bullet\bullet} \rightarrow Gd^{\bullet}_{Ba} + 2Ce_{Ce} + 6O_O \quad (7b)$$

written, equivalently, in terms of either a barium deficiency or a cerium excess.

Reaction (7) is essentially a variation of the mechanism of dopant incorporation on the "wrong" site, as proposed earlier by Kreuer [4], Equation 3. In this case, however, a barium deficiency drives the "undesirable" defect incorporation reaction, as opposed to the latter inducing an effective barium excess. In either event, dopant incorporation mechanisms and non-stoichiometry are intimately tied. In their theoretical study of perovskite zirconates, Davies *et al.* [9] calculated the solution energies of the lanthanum oxide series in $CaZrO_3$ and $SrZrO_3$. Energies for dissolution onto the A site and the M site were compared. Their results, perhaps not surprisingly, showed that smaller dopant ions were preferentially incorporated onto the M site whereas larger ions were incorporated onto the A site. In the specific case of Gd-doped barium cerate, the residence of at least some Gd on Ba sites is quite plausible as gadolinium, when in eight-fold coordination, has an ionic radius of 1.06 Å, and is 34% smaller than barium in twelve-fold coordination (1.60 Å). In comparison, Gd is 17% larger than Ce, when both are in six-fold coordination ($R[Gd_{VI}^{3+}] = 0.938$ Å, $R[Ce_{VI}^{4+}] = 0.87$ Å [14]).

The impact of barium (or strontium) deficiency on the properties of doped perovskites has not been examined as extensively as the impact of barium excess, however, several important observations have been made. Ma *et al.* found that the conductivity of Y-doped barium cerate peaked at a composition of 5 mole% Ba deficiency (regardless of atmosphere). Kreuer *et al.*, in contrast, observed a dramatic decrease in the conductivity of nominally stoichiometric La-doped barium cerate after exposure to elevated temperatures for a prolonged period (25 hrs at 1700 °C), which presumably led to BaO loss. The conductivity of 10% Ba deficient barium cerate, doped with lanthanum, was comparable. Kreuer also observed a similar result for Gd-doped barium cerate in that a barium deficiency of 10% resulted in a significant reduction in conductivity. Similarly, Nagamoto and Yamada reported the conductivity of $0.9BaO•CeO_2$ to be more than an order of magnitude lower than that of $BaCeO_3$ [15]. Shima and Haile found that compositions so deficient in barium that CeO_2 precipitates were present (i.e., $0.96BaO•0.85CeO_2•0.075Gd_2O_3$) exhibited conductivities significantly lower (by about a half an order of magnitude) than single-phase perovskite compositions. In the case of single-phase compositions, the result was temperature dependent, with Ba deficiency leading to high conductivity at low temperatures, but relatively low conductivity at high temperatures [5]. In contrast, the proton conductivity of Sr deficient doped strontium cerate ($0.95SrO•0.85ZrO_2•0.075Y_2O_3$) is reported to be more than an order of magnitude greater than that of the stoichiometric analog over the entire temperature range examined, ∼550–850° C [16].

As with the case of alkaline earth excess, alkaline earth deficiency can also have a pronounced impact on sinterability, particularly in the case of difficult to process zirconates. Ferreira found that stoichiometric $SrZr_{0.85}Y_{0.15}O_3$ densified only to 64% of theoretical density, whereas A-site deficiency, achieved either by reduction in the Sr content or addition of TiO_2, resulted in materials with densities of well over 80% of theoretical [16]. Again, it is not immediately apparent whether enhancements to the sinterability result from the presence of grain boundary phases, or increased diffusion coefficients due to point defect creation. Given the likely defect reaction of Equation 7, which consumes oxygen vacancies, it is difficult to imagine an increase in the diffusion coefficient of any species due to A-site deficiencies. It is possible that MO_2 precipitates form in the intergranular regions and serve to pin grain boundaries and prevent pore break-away, as is the case when small amounts of MgO are introduced into Al_2O_3 [17]. However, the low grain boundary mobility of zirconates would suggest that improvements in sinterability must result from enhanced rather than diminished grain growth.

2.3. Conclusions

In summary, while the details of the defect chemistry of non-stoichiometric alkaline earth perovskites remains unclear, in the majority of cases excess Ba (or Sr) results in greater sinterability and higher conductivity, but ultimately lower stability with respect to reaction with CO_2. Ba (or Sr) deficiency can similarly improve sinterability of zirconates (probably due to grain boundary pinning by ZrO_2 precipitates), but its impact on conductivity depends on the system examined. The possibility that alkaline earth deficiency may enhance stability has not been explored. The mechanism of dopant incorporation depends on the nature of the dopant, with large trivalent dopant ions exhibiting a greater tendency towards incorporation on the divalent ion site, which, in turn, leads to a lower concentration of oxygen vacancies than expected and thereby lower conductivity. The dopant incorporation mechanism is furthermore tied to the state of non-stoichiometry, with

a divalent ion deficiency driving the dopant incorporation onto the A site. Extreme processing conditions can exacerbate the situation by causing the evaporation of the alkaline earth species. Thermodynamic studies of $BaCeO_3$ by Saha and coworkers [18] indicate that the barium partial pressure under typical sintering conditions of $\sim$1600 °C can be as high as 10^{-5} atm. Ultimately, lower temperature synthetic routes will be necessary to ensure the reproducibility and optimization of the properties of proton conducting perovskite oxides.

3. Grain boundary transport

From the preceding discussion it is evident that the grain boundary chemistry is intimately linked to the bulk defect chemistry. Furthermore, it is apparent that little experimental effort has been directed at fully characterizing the grain boundaries in proton conducting perovskites. What we demonstrate here is that the overall transport properties of typical perovskites are, for all intensive purposes, insensitive to the chemistry of the grain boundaries. Thus, the wide variation in grain boundary properties that result from the variety of processing routes employed to synthesis these oxides (as exemplified by Table I) are essentially irrelevant to the macroscopic material behavior.

In a typical a.c. impedance measurement, one measures the complex impedance of a sample as a function of frequency. The real and imaginary components of the impedance are plotted in the complex plane as parametric functions of frequency. Typically, several arcs are visible in such a plot, with the arc present at high frequencies normally attributed to bulk material behavior, that present at intermediate frequencies attributed to grain boundary behavior, and that present at low frequencies attributed to electrode behavior, Fig. 2. To a first approximation, the diameter of each of these arcs corresponds to the effective d.c. resistance of each of the three regions of the material (grain interior, grain boundary, and electrode). From the knowledge of the overall sample geometry (length and area), one can convert the measured grain interior resistance to the grain interior conductivity (or resistivity). A challenge arises in the case of the grain boundaries, because the geometry of the grain boundaries (effective length and effective area) is not known a *priori*. Thus, samples with identical grain boundaries conductivities and macroscopic geometries, may yield different values of grain boundary resistance simply due to differences in microstructure.

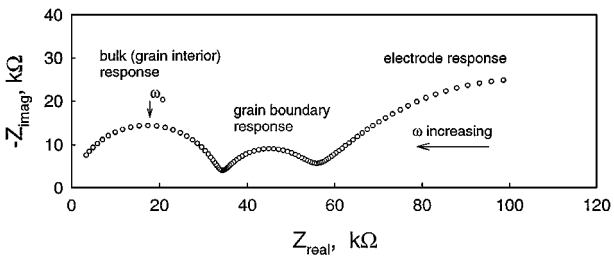

Figure 2 Schematic impedance plot in the Nyquist representation of a typical polycrystalline material.

The simplest model proposed for determining the true (or specific) grain boundary conductivity of a polycrystalline material is the "brick layer model" [11, 19–22]. More recent finite element studies indicate that the difference in values of fitted parameters between the brick layer model and a more realistic random microstructure are less than about 10%, justifying the use of the former [23]. In ref. [11] a detailed analysis of the implications of the brick layer model have been presented. There, it was concluded that if a grain boundary arc is indeed resolved in the Nyquist representation of the impedance data, even if the radius of this arc is smaller than that of the bulk (or grain interior) arc, the grain boundaries *must* have a true resistivity that is higher than that of the grain interiors. This conclusion can be demonstrated as follows. Consider the limiting case of the two-dimensional microstructure shown in Fig. 3. Four, square grains make up the polycrystalline sample, and electrodes are placed as shown. If the grain boundary conductivity is high, current will flow primarily along grain boundary (1), parallel to the grains. Thus, there will be essentially no evidence of the grain interiors in the impedance spectrum. If the grain boundary conductivity is low, current will flow primarily through the grains, but is geometrically required to traverse grain boundary (2), perpendicular to the grains. In this case, the response of both the grain boundaries and the grain interiors will be evident in the impedance spectrum. Also in this case, because the effective length of the grain boundary, δ (or $\sim n\delta$ for n grains), is much shorter than the length of the grain interiors (approximately L), the measured resistance of the grain boundary region may be smaller than that of the bulk. In this manner, a small grain boundary arc may be obtained, despite a high grain boundary resistivity.

The conclusion that the presence of a grain boundary arc immediately implies a higher grain boundary resistivity than bulk resistivity can also be arrived by another argument. The characteristic electrical frequency of a material is given by $\omega_o = 1/RC$, and corresponds to the frequency about which the arc is centered, Fig. 2. Implicit in the assignment of these arcs is the requirement that the characteristic frequency of the grain boundaries

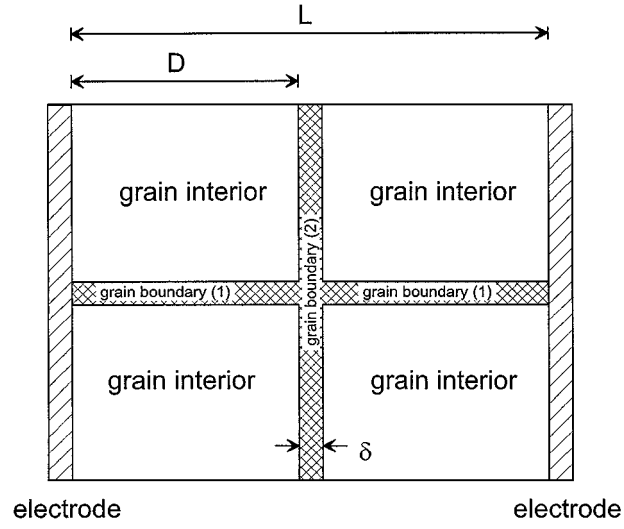

Figure 3 Limiting case of a simple microstructure.

be lower than that of the grain interiors. The characteristic frequency is, by definition, independent of the geometric shape of the material being examined, and can also be written as $\omega_o = 1/\rho\varepsilon\varepsilon_o$, where ρ is the resistivity, ε is the relative dielectric constant, and ε_o is the permittivity of vacuum. Noting that dielectric constants of ceramics do not vary nearly as much as resistivity (ignoring the effects of structural phase transitions as in $BaTiO_3$), differences in the characteristic frequencies between grain boundary and grain interior regions must be primarily due to differences in resistivity. Specifically, $\omega_{o,gb} \ll \omega_{o,gi}$ implies $\rho_{gb} > \rho_{gi}$.

Within the context of the brick layer model a semi-quantitative measure of the true grain boundary resistance can be obtained solely from the impedance data without resort to microstructural examinations. Following ref. [11] the total resistance of the grain boundaries in series with the grain interiors is

$$R_{gb} = \frac{L}{A}\left(\frac{\delta}{D}\right)\frac{1}{\sigma_{gb}}, \tag{8}$$

where L is the sample length, A is the sample cross-sectional area, δ is the grain boundary thickness, and D is the grain size. If one further assumes that the dielectric constant of the grain boundaries is approximately equal to that of the bulk, then the ratio, δ/D, is given by

$$\frac{\delta}{D} = \frac{C_{bullk}}{C_{gb}}. \tag{9}$$

Combining (8) and (9) yields

$$\sigma_{gb} = \frac{L}{A}\left(\frac{C_{bulk}}{C_{gb}}\right)\frac{1}{R_{gb}}. \tag{10}$$

Determining the dielectric constants of the grain boundary and interior regions requires one additional calculation if, as is typical, the impedance spectrum is modeled using (RQ) subcircuits rather than (RC) subcircuits, where R is a resistor, C is a capacitor and Q a constant phase element with impedance $Z_Q = [Y(j\omega)^n]^{-1}$, where $j = \sqrt{-1}$, ω is the frequency, and Y and n are constants. This additional step simply involves obtaining the effective capacitance of an (RQ) subcircuit according to [24]

$$C = Y^{1/n} R^{(1/n-l)} \tag{11}$$

Thus, all the information required for estimating the specific grain boundary conductivity is available from the impedance measurement.

The approach outlined here has been applied to $BaCe_{0.85}Gd_{0.15}O_3$ [11]. In Fig. 4 the impedance spectra of several samples, prepared by solid state reaction and sintered at temperatures between 1400 and 1700 °C are shown. The spectra were collected at 100 °C under water-saturated argon. At first glance it appears that the grain boundary resistivity is lower than that of the bulk, particularly for the sample sintered at 1700 °C, and might even prompt one to pursue nanocrystalline

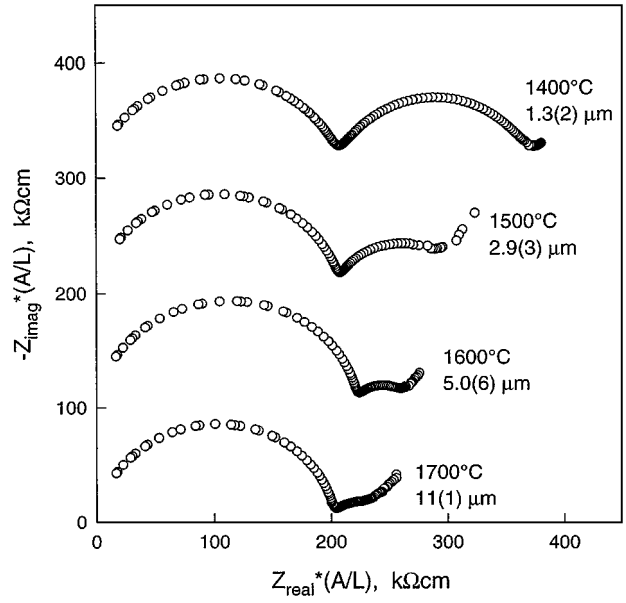

Figure 4 Impedance spectra collected from $BaCe_{0.85}Gd_{0.15}O_3$ at 100°C under H_2O saturated argon. Sintering temperature and mean grain size of each sample as indicated.

materials as a method of reducing the total resistivity of the material. Closer examination of these materials, however, reveals that the sample sintered at 1700 °C has larger grains (~10 μm), and exhibits a lower grain boundary resistance simply because fewer boundaries are encountered by the mobile charge carriers. In the case of the sample sintered at 1400 °C, the mean grain size is 1.3 μm, and grain boundaries, despite occupying a small volume fraction of the overall sample, cause as much resistance to ion transport as the bulk. Taking the microstructure into account as described above, the specific grain boundary conductivity for each of the materials is on the order of $1.5 \times 10^{-8}\ \Omega^{-1}\ cm^{-1}$. This value is independent of grain size (for the set of samples represented in Fig. 4) and several orders of magnitude lower than the bulk conductivity of $5 \times 10^{-6}\ \Omega^{-1}\ cm^{-1}$. Other noteworthy properties of grain boundaries in proton conducting perovskites include (1) charge transport by protons, as demonstrated by higher grain boundary conductivity under H_2O than D_2O saturated atmospheres, (2) greater responsiveness within the grain boundary regions to changes in atmosphere, and (3) higher water concentrations within the intergranular regions than within the bulk.

This study of $BaCe_{0.85}Gd_{0.15}O_3$ suggests that large-grained materials are necessary in order to minimize total resistance. It should be noted, however, than in all cases where grain boundary conductivity in proton conducting perovskites has been studied, the activation energy for transport through grain boundaries is higher than that for transport through the bulk. Consequently, at temperatures of 300–400 °C and above, even for small-grained materials, the arc associated with grain boundary resistance becomes exceedingly small and no longer contributes to the total material resistance. Thus, for typical fuel cell operating temperatures, the electrolyte microstructure will not effect its impedance. While proton transport along grain boundaries may not

be critical to the electrical behavior of perovskites, grain boundaries may play an important role in the molecular diffusion of water, as evidenced by the faster rate of $H_2O \leftrightarrow D_2O$ exchange in polycrystalline samples of $BaCe_{0.85}Gd_{0.15}O_3$ than in single crystals [25].

4. Chemical stability

4.1. Thermodynamic studies

The high proton conductivities of doped $BaCeO_3$ and $SrCeO_3$ render them attractive for many applications. They have not been widely implemented, however, because they suffer from poor chemical stability. In particular, barium cerate can react with CO_2 according to reaction (12), or with H_2O according to reaction (13).

$$BaCeO_3 + CO_2 \rightarrow BaCO_3 + CeO_2 \quad (12)$$

$$BaCeO_3 + H_2O \rightarrow Ba(OH)_2 + CeO_2 \quad (13)$$

Reaction (13) is not relevant at the high temperatures of operation expected for a fuel cell [26], and thus the remainder of the discussion is limited to reaction (12).

The reaction of an AMO_3 perovskite with CO_2, as given for $BaCeO_3$ above, can be broken into two reactions involving the individual metal oxides:

$$AMO_3 \rightarrow AO + MO_2 \quad (14)$$

$$AO + CO_2 \rightarrow ACO_3 \quad (15)$$

The energetics of reaction (15) are well established for all the alkaline earth elements. Reaction (14) has also been widely studied in the context of the crystal chemistry of perovskites.

At the standard state of $T = 298.15$ K and $P = 1$ atm, the Gibbs free energies of reaction (15) to form $BaCO_3$ and $SrCO_3$, respectively, are [27]

$$\Delta G^{o}_{rxn}(15) = -268 \text{ kJ/mol} + (0.17 \text{ kJ/mol*K})*T$$

and

$$\Delta G^{o}_{rxn}(15) = -234 \text{ kJ/mol} + (0.17 \text{ kJ/mol*K})*T.$$

Because the enthalpy and entropy of formation of the component species involved in reaction (15) do not vary by more than a few per cent over the temperature range from 298.15 K to – 1000 K [27], these ΔG values can be used to evaluate the thermodynamic stability of the alkaline earth perovskites even at the high temperature of operation of a fuel cell.

Turning to reaction (14), several authors have noted that ΔH^{o}_{rxn} for the formation of perovskites from the individual oxides shows a correlation with the perovskite tolerance factor, t, Fig. 5 [28]. This structural parameter, defined as

$$t = (R_A + R_O)/2^{1/2}(R_M + R_O),$$

describes the extent of distortion of the perovskite structure from the ideal cubic aristotype due to mismatch between the A-O and M-O bond lengths. The energetics

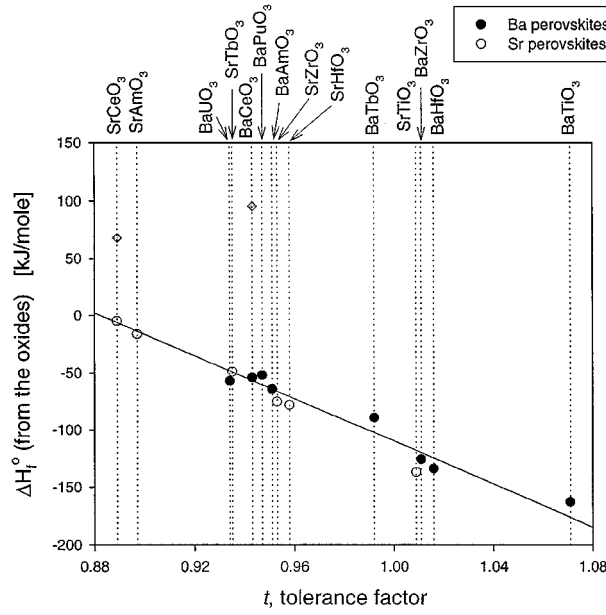

Figure 5 The negative of the enthalpy of reaction (14) plotted as a function of perovskite tolerance factor (see text). Anomalous data for $BaMoO_3$ and $BaPrO_3$, which lie far above and below the linear regression line, respectively, and have not been reproduced in other laboratories, have been omitted.

of the formation of the specific compounds of interest, $BaCeO_3$ and $SrCeO_3$ (and the analogous zirconates), have been studied by several independent groups and the results are summarized in Table II. In the case of the calorimetric studies, the measured parameters reflect the formation of the perovskite from the component elements (as opposed to the oxides). The corresponding thermodynamic functions for reaction (14) can be calculated by accounting for the formation energies of the individual oxides:

$$\Delta G^{o}_{f}(BaO) = -554 \text{ kJ/mol} + (0.09 \text{ kJ/mol*K})*T,$$

$$\Delta G^{o}_{f}(SrO) = -592 \text{ kJ/mol} + (0.10 \text{ kJ/mol*K})*T,$$

$$\Delta H^{o}_{f}(CeO_2) = -1089 \text{ kJ/mol [34]},$$

and

$$\Delta G^{o}_{f}(ZrO_2{-}m) = -1079 \text{ kJ/mol} + (0.13 \text{ kJ/mol*K})*T$$

where these values are taken from Barin [27], unless otherwise noted.

In the case of the galvanostatic measurements of the cerates [32], the constructed cell directly yielded the energetics of the reaction of the perovskite with CO_2 (reaction 12), from which it is possible to obtain the $\Delta G^{o}_{rxn}(14)$ by accounting for the formation energies of the alkaline earth carbonates (given above).

The data summarized in Fig. 5 demonstrate that, generally, the stability of the perovskite structure increases with increasing tolerance factor, i.e., as the distortion from the cubic aristotype decreases. Notable exceptions are two data points with positive - $\Delta H_{rxn}(14)$ for $BaCeO_3$ and $SrCeO_3$ as determined by Gopalan and Virkar [32]. The discrepancy between these results and those of the calorimetric measurements for cerates

TABLE II Thermodynamic parameters for the reaction: $AO + MO_2 \rightarrow AMO_3$ for the standard state T = 298.15 K and P = 1 atm (zirconia in monoclinic phase)

AMO_3	ΔH_r^o kJ/mol	ΔS_r^o kJ/mol K	Method	Source
$BaCeO_3$	−54	n/a	solution calorimetry	Goudiakas *et al.* [29]
	−57	n/a	solution calorimetry	Cordfunke *et al.* [30]
	−52	n/a	solution calorimetry	Morss & Mensi [31]
	−49[a]	n/a	differential calorimetry	Saha *et al.* [18]
	−54	*n/a*	*prefered value*	
	95	0.11	galvanic cell	Gopalan & Virkar [32]
$SrCeO_3$	−5	n/a	solution calorimetry	Goudiakas *et al.* [29]
	−6	n/a	solution calorimetry	Cordfunke *et al.* [30]
	68	0.11	galvanic cell	Gopalan & Virkar [32]
	−5	*n/a*	*prefered value*	
$BaZrO_3$	−128	0.002	galvanic cell	Jacob & Wasseda [33]
$SrZrO_3$	−74	0.015	galvanic cell	Jacob & Wasseda [33]

[a] ΔG_r^o at 1000°C

TABLE III Thermodynamic parameters for the reaction: $AMO_3 + CO_2 \rightarrow ACO_3 + MO_2$ for the standard state $T = 298.15$ K and $P = 1$ atm (zirconia in monoclinic phase). Values determined by combining parameters for reaction (14) given in Table II with parameters for reaction (15) given in text [27]

AMO_3	ΔH_r^o kJ/mol	ΔS_r^o kJ/mol K	Method	Source
$BaCeO_3$	−214	n/a	*preferred value*	see Table II
	−357	−0.268	galvanic cell[a]	Gopalan & Virkar [32]
$SrCeO_3$	−229	n/a	*preferred value*	see Table II
	−298	−0.262	galvanic cell[a]	Gopalan & Virkar [32]
$BaZrO_3$	−140	−0.17	galvanic cell	Jacob & Waseda [33]
$SrZrO_3$	−160	−0.18	galvanic cell	Jacob & Waseda [33]

[a] Thermodynamic parameters for the reaction of the perovskite with the carbonate measured directly.

cannot be easily resolved. The weight of the experimental evidence suggests that the enthalpy of formation from the oxides for both $BaCeO_3$ and $SrCeO_3$ should be negative as determined calorimetrically. Significantly, whether one utilizes the calorimetric or galvanostatic data, the enthalpy of reaction for the formation of the carbonate from the perovskite is nevertheless negative, Table III. A negative $\Delta H_{rxn}(12)$ implies that at low temperatures carbonate formation is favored over the formation of the perovskite, which is very much in agreement with experimental observations. Indeed, several authors have reported that strontium and barium cerates can "crumble" after several days of exposure to atmospheric CO_2 at ambient temperatures, a serious drawback for technological applications of these materials.

4.2. $ACeO_3 - AZrO_3$ solid solution systems

From the data presented in Table III one can expect the zirconates, especially $BaZrO_3$, to be much more stable against carbonate formation than the cerates, and thus much more desirable for applications in fuel cell environments. Early measurements of the conductivity of doped zirconates suggested that their proton conductivity was very low, $\sim 1.3 \times 10^{-6}$ S/cm at 600 °C under moist N_2 in the case of $BaZr_{0.9}Y_{0.1}O_3$ [35] and $\sim 3.2 \times 10^{-4}$ S/cm in the case of $BaZr_{0.95}Y_{0.05}O_3$ [36] at the same temperature but under pure hydrogen. A recent quantum molecular dynamics study furthermore indicated that the barrier to proton transport in $BaZrO_3$ should be greater than that in $BaCeO_3$ [37], consistent with these observations of low conductivity. Accordingly, one strategy that has emerged for developing perovskites of both high proton conductivity and high chemical stability is the exploration of the $AZrO_3 - ACeO_3$ pseudo-binary systems. It should be noted, however, that very recent investigations of $BaZrO_3$ suggest that the solubility of protons in this compound is much higher than previously reported, and it may, in fact, have a conductivity comparable to that of $BaCeO_3$ [38, 39].

The perovskites $BaZrO_3$ and $BaCeO_3$ are not isostructural at room temperature; the zirconate is cubic, space group P*m*3*m* [40], whereas the cerate exhibits an orthorhombic distortion, space group P*nma*, with $|a_{ortho}| \approx |b_{ortho}| \approx \sqrt{2}|a_{cubic}|$, and $|c_{ortho}| \approx 2|a_{cubic}|$ [41]. Charrier-Cougoulic *et al.* studied the crystal chemistry of the (undoped) $BaZrO_3$ – $BaCeO_3$ system by Raman spectroscopy and X-ray diffraction and found that the structure evolves from cubic (P*m*3*m*) to rhombohedral (*R*3*c*) to centered orthorhombic (I*mma*) to primitive orthorhombic (P*nma*) with increasing cerium content [42]. The reverse sequence of transitions is observed for the end-member cerate with increasing temperature [41]. No two-phase regions were identified in the zirconate-cerate system, and, somewhat surprisingly, the pseudo-cubic lattice constant was found to vary linearly with composition over the entire composition range. In the case of doped compositions, a linear variation of lattice constant with Zr content is also observed. The $SrZrO_3$ – $SrCeO_3$ system exhibits a similarly linear relationship between lattice constants and composition [43].

Electrical measurements of compounds in both the $BaZrO_3$ – $BaCeO_3$ and the $SrZrO_3$ – $SrCeO_3$ systems generally reveal a monotonic decrease in conductivity (under H_2O saturated argon) as the zirconium content is increased. Matzke and Cappadonia obtained this result for 5 mole% Yb-doped strontium cerate-zirconate over the entire composition range from $SrCe_{0.95}Yb_{0.05}O_3$ to $SrZr_{0.95}Yb_{0.05}O_3$ [43]. Sata *et al.* [44] have examined the identical system and obtained somewhat contradictory results, however, this could be a consequence of their synthetic procedure. Samples were prepared

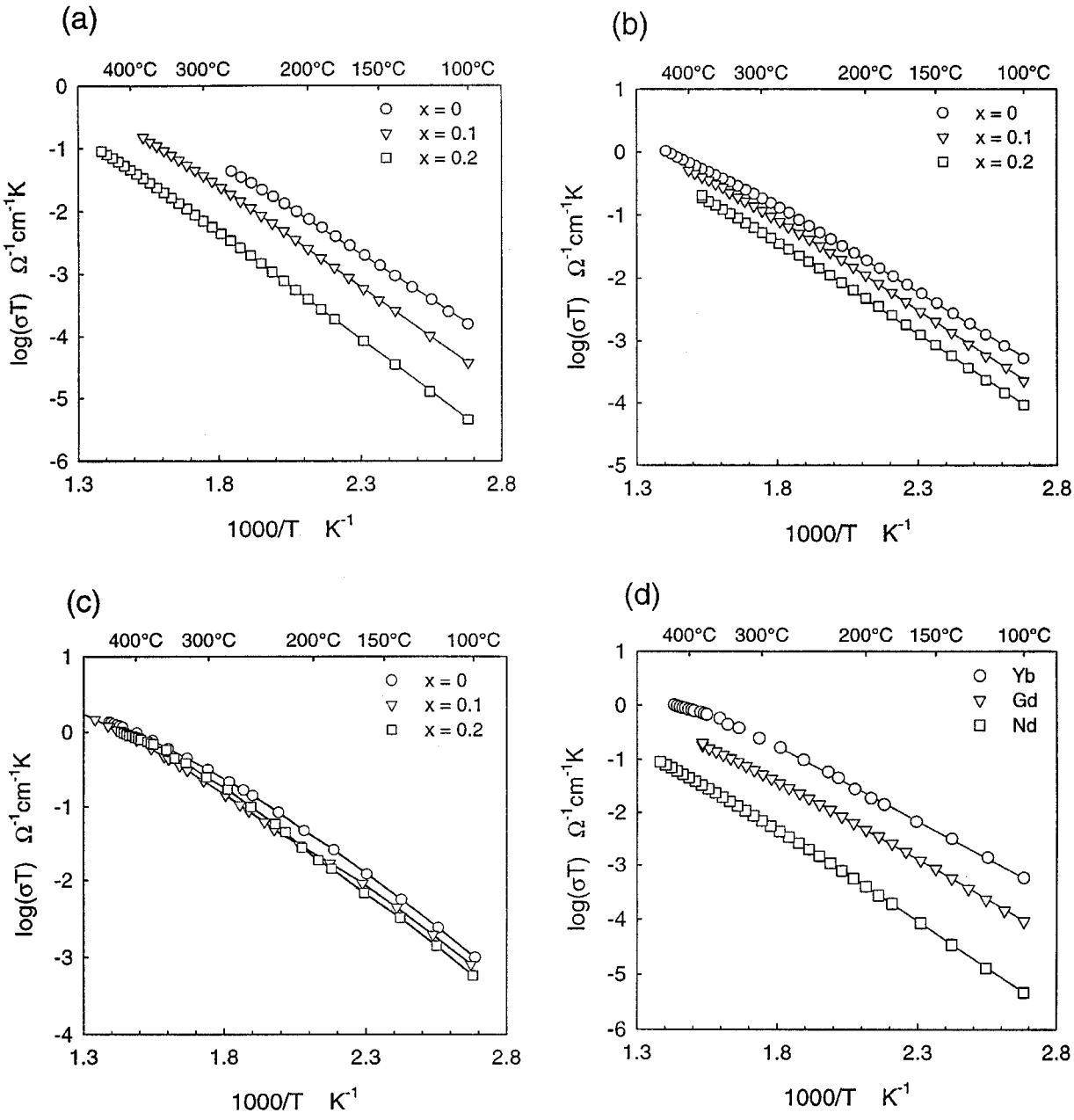

Figure 6 The conductivity of $BaCe_{0.9-x}Zr_xM_{0.1}O_3$ under H_2O saturated argon; (a) M = Nd; (b) M = Gd; (c) M = Yb; (d) X = 0.2.

from the melt, which likely led to vaporization of the alkaline earth species, as is the case for melt growth of $BaCeO_3$ [11, 45]. Electrical results from the authors' laboratory for the barium cerate- zirconate system with Gd, Nd and Yb as dopant species are shown in Fig. 6. The materials were prepared by solid state reaction as described in ref. [46] and characterized by X-ray powder diffraction and a.c. impedance spectroscopy under H_2O saturated argon. Samples were sintered at temperatures of 1500–1650 °C after cold-isostatic pressing. Only those with Zr contents of $\leq$20% densified to a degree satisfactory for conductivity measurements ($\rho \geq 92\%\rho_{theo}$).

The data in Fig. 6 demonstrate that not only does the introduction of Zr into barium cerate cause a decrease in conductivity, its impact increases in the order Yb $\rightarrow$ Gd $\rightarrow$ Nd. That is, while the conductivity of $BaCe_{0.9-x}Zr_xNd_{0.1}O_{3-\delta}$ decreases by more than order of magnitude between $x = 0$ and $x = 0.2$, the conductivity of the Yb-doped perovskite is hardly affected over the analogous composition range. Moreover, the conductivity for a given Zr content follows the identical chemical sequence with $\sigma(Yb) > \sigma(Gd) > \sigma(Nd)$. This last observation is in agreement with earlier measurements by Stevenson *et al.* [47] of the conductivity of doped barium cerate at low temperatures (<400 °C). We interpret these conductivity results as follows. It was noted above that larger dopant ions have a greater tendency to incorporate onto the divalent ion site and thus give rise to fewer oxygen vacancies than smaller dopant ions. Such behavior immediately explains the high conductivity of Yb doped compositions. As the average ionic radius of the tetravalent ion decreases, that is as Zr is introduced, one expects a greater proportion of the large dopant ions to reside on the divalent ion site and thus the large impact of introducing Zr into Nd doped barium cerate. In contrast, ytterbium, which is the same size as cerium (0.868 Å in radius as compared to 0.870 Å) is simply too small for the divalent ion site, even in the presence of the small Zr^{4+} (0.72 Å) ion.

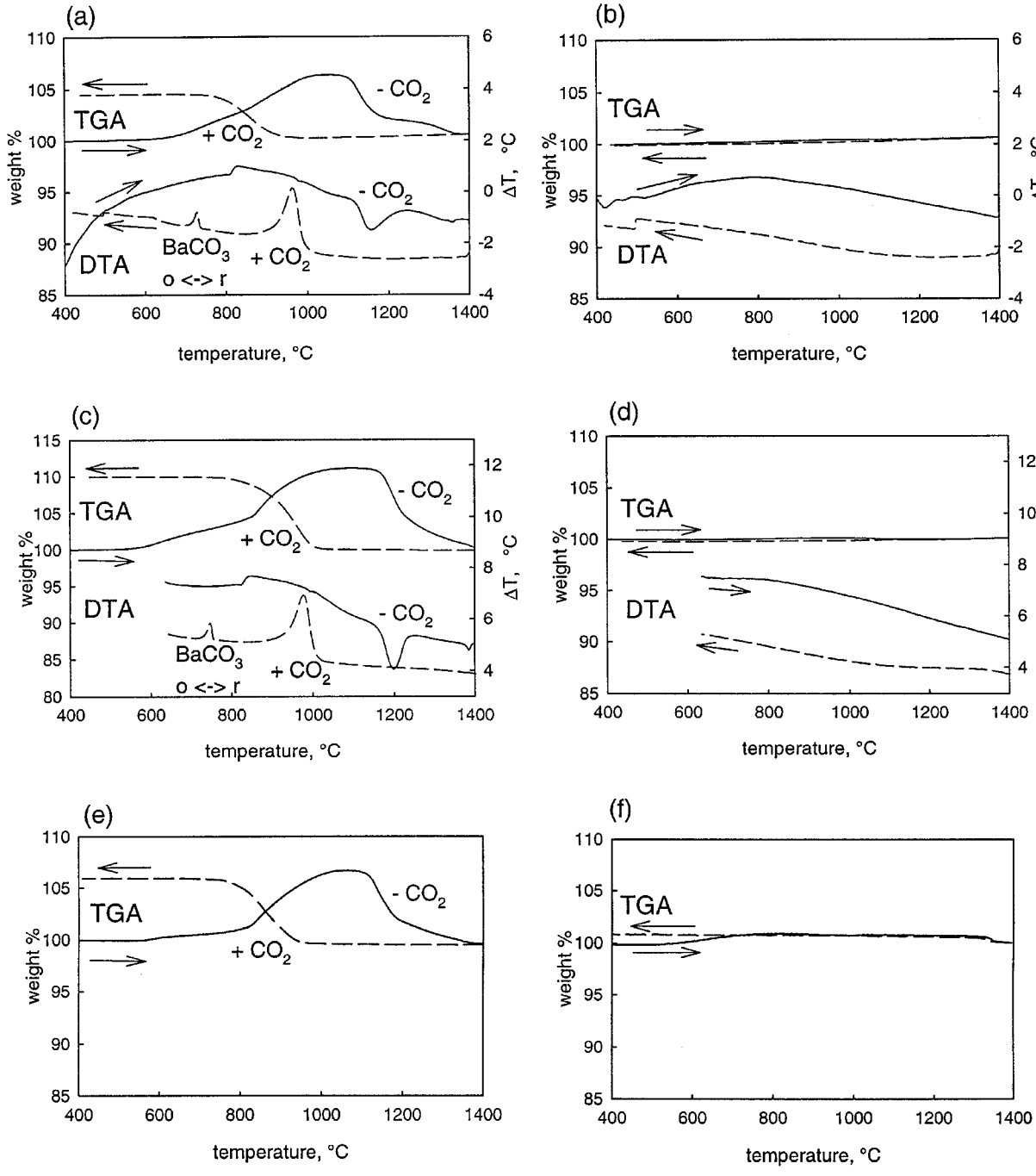

Figure 7 Thermal gravimetric (TGA) and differential thermal (DTA) traces collected from $BaCe_{0.9-x}Zr_xM_{0.1}O_3$ under flowing CO_2 at a heating rate of 20°C/min: (a) $BaCe_{0.9}Nd_{0.1}O_3$, (b) $BaCe_{0.7}Zr_{0.2}Nd_{0.1}O_3$, (c) $BaCe_{0.9}Gd_{0.1}O_3$, (d) $BaCe_{0.5}Zr_{0.4}Gd_{0.1}O_3$, (e) $BaCe_{0.9}Yb_{0.1}O_3$, and (f) $BaCe_{0.5}Zr_{0.4}Yb_{0.1}O_3$.

Therefore, introducing zirconium into Yb doped compositions has little effect on the conductivity. Gadolinium, being of intermediate ionic radius between Nd and Yb [14], gives rise to intermediate behavior.

As might be anticipated, the stability of $BaCe_{1-x}Zr_xO_3$ compounds increases with increasing x. Selected thermal gravimetric and thermal differential data showing the behavior of doped compositions in this system under flowing CO_2 are presented in Figs. 7 and 8, and summarized in Fig. 9 in terms of the percentage of Ba atoms converted to $BaCO_3$ at the peak of weight gain. While the compositions bearing no Zr clearly reacted with CO_2, the Gd-doped composition containing 40% Zr and the Nd-doped composition containing 20% Zr did not react within the time frame of the experiment. In the case of the Yb-doped materials, at the highest Zr content examined, 40 mole%, the reactivity with CO_2 was reduced to $\sim$ 4 mole% of Ba. A somewhat unanticipated result is the effect of calcination temperature, evident in Figs. 8 and 9, with higher calcination temperatures leading to greater stability. This can be explained by the greater chemical homogeneity of compositions calcined at higher temperatures, as confirmed by transmission electron microscopy. These observations strongly suggest chemical stabilization of perovskite cerates by Zr introduction may ultimately be even greater than indicated in Figs. 7 and 9, if we can ensure a high degree of homogeneity. Compositional homogeneity may, in turn, may be achieved by chemical synthesis of the perovskites.

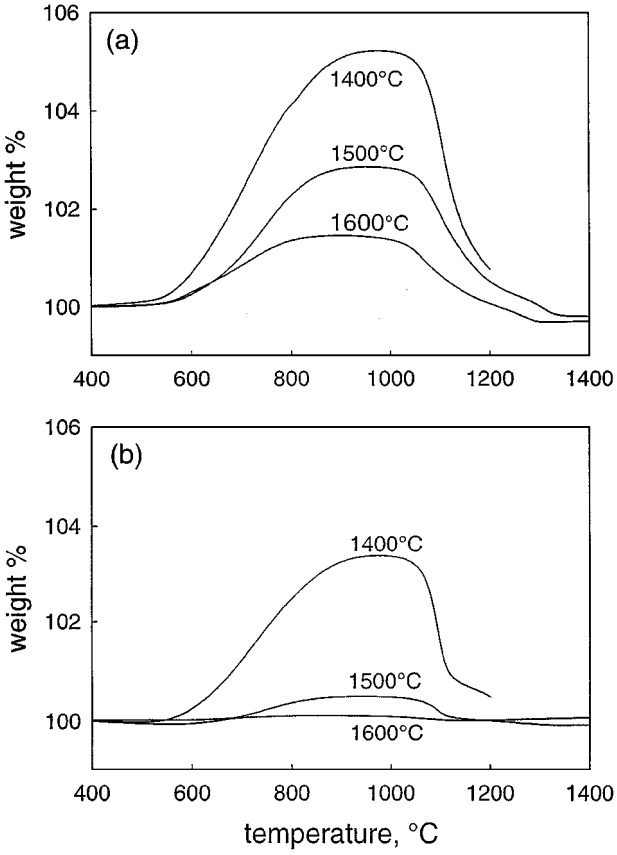

Figure 8 Thermal gravimetric traces collected from (a) $BaCe_{0.8}Zr_{0.1}Nd_{0.1}O_3$ and (b) $BaCe_{0.7}Zr_{0.2}Gd_{0.1}O_3$ calcined at the temperatures indicated.

5. Summary

The questions of bulk defect chemistry, non-stoichiometry, grain boundary chemistry, chemical stability and processing of proton conducting perovskites are intricately tied to one another. Loss of the alkaline earth species at high temperature, for example, can lead to trivalent dopant ion "transfer" from the tetravalent to the divalent ion site, which in turn, will reduce the concentration of oxygen vacancies. Similarly, intentional deviations from stoichiometry strongly impact both the sintering behavior and chemical stability. The number of firm conclusions that can be drawn regarding the behavior of proton conducting perovskites in response to subtle changes in chemistry and processing conditions is not as high as one would like, because of significant literature discrepancies. It is quite evident, however, that grain boundaries in perovskites do not provide a pathway for fast proton transport. Furthermore, the $ACeO_3 - AZrO_3$ system continues to be a very promising route to obtaining materials of both high conductivity and high stability. Areas in which significant experimental efforts will be required in order to completely understand the behavior of proton conducting perovskites are direct observations of dopant incorporation sites and low temperature processing routes that preserve the material chemistry. Given the potential impact of high chemical stability and high proton conductivity oxides on a wide range of electrochemical devices, in particular fuel cells and H_2O electrolysis cells, efforts in these areas are certainly well justified.

Appendix

Methods of accomodating AO excess in perovskites:

$$AO \rightarrow A_i^{\bullet\bullet} + O_i'' \quad (1)$$

$$AO \rightarrow A_A + O_O + V_M'''' + 2V_O^{\bullet\bullet} \quad (2)$$

$$2AO \rightarrow A_A + A_M'' + 2O_O + V_O^{\bullet\bullet}. \quad (3)$$

To evaluate ΔE for (1):

$$A_A \rightarrow V_A'' + A_i^{\bullet\bullet} \quad (4)$$

$$O_O \rightarrow V_O^{\bullet} + O_i'' \quad (5)$$

$$A_A + O_O \rightarrow V_A'' + V_O^{\bullet\bullet} + AO \quad (6)$$

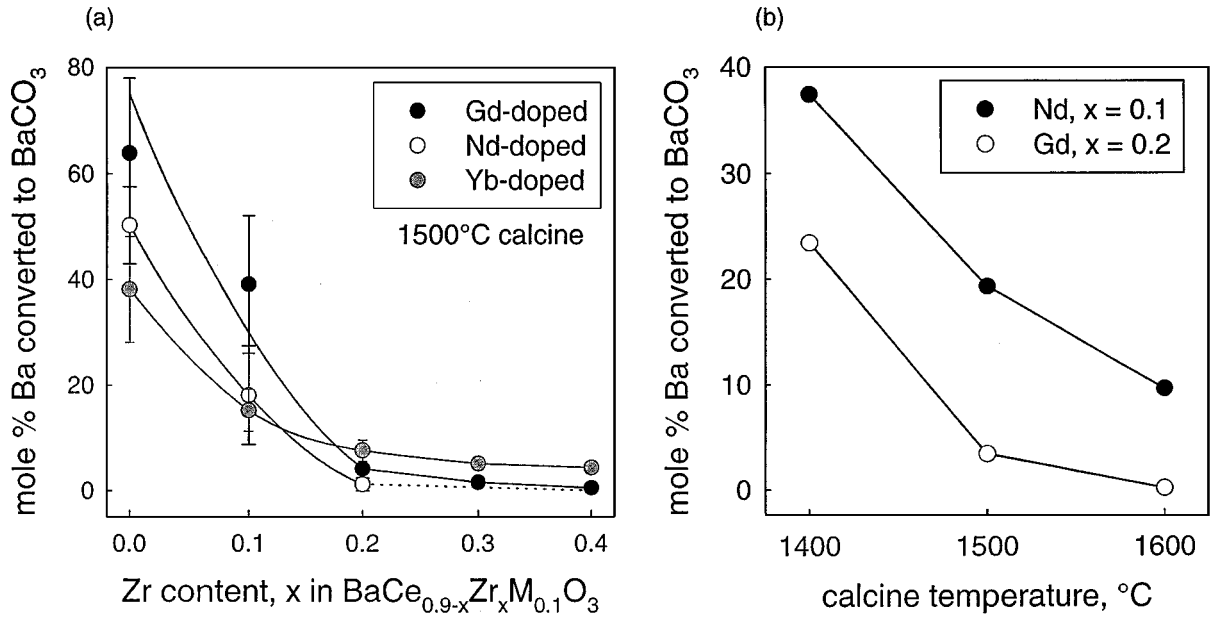

Figure 9 Maximum mole percent of barium in $BaCe_{0.9-x}Zr_xM_{0.1}O_3$ converted to $BaCO_3$ during TGA examination, as determined by the maximum weight gain upon heating.

$$\Delta E(1) = \Delta E(4) + \Delta E(5) - \Delta E(6)$$

$$\Delta E(1, SrZrO_3) \sim 8 \text{ eV/defect};$$

$$\Delta E(1, CaZrO_3) \sim 5.6 \text{ eV/defect}$$

To evaluate ΔE for (2):

$$A_A + M_M + 3O_O \rightarrow V''_A + V''''_M + 3V^{\bullet\bullet}_O + AMO_3 \quad (7)$$

$$\text{null} \rightarrow V''_A + V''''_M + 3V^{\bullet\bullet}_O \quad (8)$$

$$A_A + O_O \rightarrow V''_A + V^{\bullet\bullet}_O + AO \quad (6)$$

$\Delta E(2) = \Delta E(7) - \Delta E(6)$, assuming (7) and (8) are equivalent.

$$\Delta E(2, SrZrO_3) \sim 0.7 \text{ eV/defect};$$

$$\Delta E(2, CaZrO_3) \sim 1 \text{ eV/defect}$$

To evaluate ΔE for (3):

$$AO \rightarrow A_A + O_O + V''''_M + 2V^{\bullet\bullet}_O \quad (2)$$

$$AO + V''''_M + V^{\bullet\bullet}_O \rightarrow A''_M O_O \quad (9)$$

$\Delta E(3) = \Delta E(2) + \Delta E(9)$, but $\Delta E(9)$ is unknown.

Acknowledgements

The authors gratefully acknowledge the support of the Irvine Foundation, Hughes Research Labs and the National Science Foundation via a National Young Investigator award. The authors also thank Dr. M.S. Islam for insightful discussions and Dr. Carol Garland for assistance with transmission electron microscopy.

References

1. H. IWAHARA, T. ESAKA, H. UCHIDA and N. MAEDA, *Solid State Ionics* **3/4** (1981) 359.
2. N. FUKATSU, N. KURITA, T. YAJIMA, K. KOIDE K and T. OHASHI, *J. Alloy Compd.* **231** (1995) 706.
3. H. IWAHARA, T. YAJIMA, T. HIBINO and H. USHIDA, *J. Electrochem. Soc.* **140** (1993) 1687.
4. K. D. KREUER, E. SCHÖNHERR and J. MAIER, in Proceedings of the 14th Risø International Symposium on Materials Science, Risø Natl. Lab., Roskilde, Denmark, 1993.
5. D. SHIMA and S. M. HAILE, *Solid State Ionics* **97** (1997) 443.
6. J. GUAN, S. E. DORRIS, U. BALACHANDRAN and M. LIU, *J. Electrochem. Soc.* **145** (1998) 1780.
7. G. MA, T. SHIMURA and H. IWAHARA, *Solid State Ionics* **110** (1998) 103.
8. G. MA, H. MATSUMOTO and H. IWAHARA, *ibid.* **122** (1999) 237.
9. R. A. DAVIES, M. S. ISLAM and J. D. GALE, *ibid.* **126** (1999) 323.
10. A. S. NOWICK and Y. DU, *ibid.* **77** (1995) 137.
11. S. M. HAILE, D. WEST and J. CAMPBELL, *J. Mater. Res.* **13** (1998) 1576.
12. F. KRUG, T. SCHOBER, R. PAUL and T. SPRINGER, *Solid State Ionics* **77** (1995) 185.
13. J. LUYTEN, F. DE SCHUTTER, J. SCHRAM and J. SCHOONMAN, *ibid.* **46** (1991) 117.
14. R. D. SHANNON, *Acta Cryst A* **32** (1976) 751.
15. H. NAGAMOTO and H. YAMADA, in Proceedings of the 2nd International Symposium on Ionic and Mixed Conducting Ceramics, San Francisco, 1994, edited by T. A. Ramanarayanan, W. L. Worrell and H. L. Tuller (The Electrochemical Society, Pennington, NJ, 1994) p. 39.
16. A. A. FERREIRA, J. A. LABRINCHA and J. R. FRADE, *Solid State Ionics* **77** (1995) 210.
17. D. W. RICHARDSON, in "Modern Ceramic Engineering," 2nd ed. (Marcel Dekker, Inc., New York, 1992) p. 528.
18. R. SAHA, R. BABU, K. NAGARAJAN and C.K. MATHEWS, *Thermochimica Acta* **120** (1987) 29.
19. N. BONANOS, B. C. H. STEELE and E. P. BUTLER, in "Impedance Spectroscopy," edited by J. R. MacDonald (Wiley and Sons, New York, USA, 1988) p. 191.
20. H. NAFE, *Solid State Ionics* **13** (1984) 255.
21. X. GUO and R.-Z. YUAN, *J. Mater. Sci. Lett.* **14** (1995) 499.
22. G. M. CHRISTIE and F. P. F. VAN BERKEL, *Solid State Ionics* **83** (1996) 17.
23. J. FLEIG and J. MAIER, *J. Electrochem. Soc.* **145** (1998) 2081.
24. J. R. MACDONALD and W. B. JOHNSON, in "Impedance Spectroscopy," edited by J. R. MacDonald (Wiley and Sons, New York, 1988) p. 1.
25. D. L. WEST, M.S. Thesis, University of Washington, 1996 p. 72.
26. K. D. KREUER, *Solid State Ionics* **97** (1997) 1.
27. I. BARIN, "Thermochemical Data of Pures Substances: Vols 1 & 2" (VCH Publishers, New York, 1989).
28. E. TAKAYAMA-MUROMACHI and A. NAVROTSKY, *J. Solid State Chem.* **72** (1988) 244.
29. J. GOUDIAKAS, R. G. HAIRE and J. FUGER, *J. Chem. Thermodynamics* **22** (1990) 577.
30. E. H. P. CORDFUNKE, A. S. BOOIJ and M. E. HUNTELAAR, *ibid.* **30** (1998) 437.
31. L. R. MENSCH and N. MENSI, in Proceedings of the 15th Rare Earth Research Conference, June 15–18, 1981, Univ. of Missouri, Rolla, edited by G. J. McCarthy and J. J. Rhyne (Plenum Press, New York, 1982) p. 279.
32. S. GOPALAN and A. V. VIRKAR, *J. Electrochem. Soc.* **140** (1993) 1060.
33. K. T. JACOB and Y. WASEDA, *Met. Mat. Trans.* **26B** (1995) 775.
34. L. R. MORSS, *J. Less Comm. Met.* **93** (1983) 301.
35. R. T. C. SLADE, S. D. FLINT and F. SINGH, *Solid State Ionics* **82** (1995) 135.
36. H. IWAHARA, T. YAJIMA, T. HIBINO, K. OZAKI and H. SUZUKI, *ibid.* **61** (1993) 65.
37. W. MÜNCH, G. SEIFERT, K. D. KREUER and J. MAIER, *ibid.* **97** (1997) 39.
38. K. D. KREUER, *ibid.* **125** (1999) 285.
39. H. G. BOHN and T. SCHOBER, *J. Amer. Ceram. Soc.* **83** (2000) 768.
40. M. D. MATHEWS, E. B. MIZRA and A. C. MOMIN, *J. Mater. Sci. Lett.* **10** (1991) 305.
41. K. S. KNIGHT, *Solid State Ionics* **74** (1994) 109.
42. I. CHARRIER-COUGOULIC, T. PAGNIER and G. LUCAZEA, *J. Solid State Chem.* **142** (1999) 220.
43. T. MATZKE and M. CAPPADONIA, *Solid State Ionics* **86–88** (1996) 659.
44. N. SATA, H. YUGAMI, Y. AKIYAMA, H. SONE, N. KITAMURA, T. HATTORI and M. ISHIGAME, *ibid.* **125** (1999) 383.
45. D. WEST, S. M. HAILE and R. S. FEIGELSON, *Mat. Res. Soc. Symp. Proc.* **393** (1995) 31.
46. K. H. RYU and S. M. HAILE, *Solid State Ionics* **125** (1999) 355.
47. D. A. STEVENSON, N. JIANG, R. M. BUCHANAN and F. E. G. HENN, *ibid.* **62** (1993) 279.

Received 22 June
and accepted 17 August 2000